

pubs.acs.org/NanoLett Letter

Solution-Processed Temperature-Adaptive Radiative Paint as a Thermal Imaging Sensitizer

Kai Xu, Jiachen Li, Finnegan G. Reichertz, Ruihan Guo, Nawel S. Khelfallah, Rui Zhang, Ali Javey, Rayne Zheng, and Junqiao Wu*

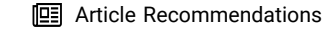


Cite This: Nano Lett. 2025, 25, 14953-14959



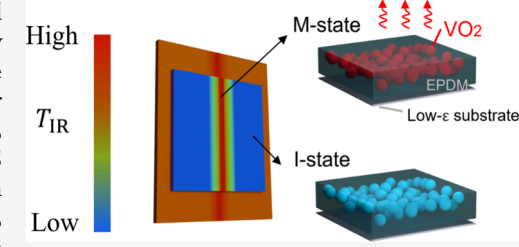
ACCESS I

III Metrics & More



Supporting Information

ABSTRACT: Thermography detects mid-infrared radiation from surfaces based on the Stefan-Boltzmann law, mapping surface temperatures and potentially revealing subsurface thermal activity. Recent developments offer an alternative strategy to traditional camera-based improvements: a thermal imaging sensitizer (TIS) coating whose emissivity increases sharply with local temperature, amplifying small thermal variations into high-contrast signals. Existing TIS structures are nanofabricated solid membranes and face significant challenges in fabrication complexity. Here, we present a solution-processed, liquid form of TIS, termed temperature-adaptive radiative paint (TARP), to address these limitations. TARP offers drastically reduced fabrication costs, scalability to



large areas, applicability to curved surfaces, and an extended operating temperature range, while maintaining the function of temperature amplification. Application of TARP enhances small temperature contrast by more than 3 times, substantially improving ambient thermography and enabling broader applications such as detection of structural defects and hot spots in electronic components.

KEYWORDS: vanadium dioxide, phase change materials, thermography, paint, plasmonics

Thermography uses infrared (IR) cameras to map the temperature distribution of object surface by detecting mid-IR thermal radiation. The infrared temperature ($T_{\rm IR}$) is calculated from the detected radiation using the Stefan–Boltzmann law. For calibration, a constant, wavelength-integrated emissivity (ε_0) is typically preset for IR cameras, which is commonly set to \sim 0.95, the approximate emissivity of most nonmetallic materials. This assumption enables temperature readings in most practical applications.

However, if the actual emissivity (ε) differs substantially from ε_0 or even becomes strongly temperature-dependent, $T_{\rm IR}$ will deviate from the true temperature T. Following the relation of radiated power $P_{rad} = \varepsilon_0 \ \sigma T_{IR}^4 = \varepsilon \sigma T^4$, where $\sigma = \frac{2\pi^5 k_{\rm B}^4}{15\varepsilon^2 h^3}$ is the Stefan–Boltzmann constant, differentiating $T_{\rm IR}$ with respect to T gives²

$$\frac{\mathrm{d}T_{\mathrm{IR}}}{\mathrm{d}T} = \left(\frac{\varepsilon}{\varepsilon_0}\right)^{1/4} \left(1 + \frac{1}{4} \frac{\mathrm{d}\ln\varepsilon}{\mathrm{d}\ln T}\right) \tag{1}$$

For conventional materials, emissivity remains nearly constant with moderate temperature change of ~20 °C, so $dT_{\rm IR}/dT$ is only weakly temperature dependent. However, by combining phase change materials with photonic structures, one can design a coating whose emissivity increases sharply with temperature within the temperature window of phase transition. As a result, such a sharply rising $\varepsilon(T)$ amplifies the small variation in actual surface temperature (dT) into a larger

contrast of $\mathrm{d}T_{\mathrm{IR}}$ seen by the camera, and $\mathrm{d}T_{\mathrm{IR}}/\mathrm{d}T$ far exceeds one (Figure 1B). The distribution of true surface temperature, T(x,y), can be accurately retrieved by calibrating the recorded map of $T_{\mathrm{IR}}(x,y)$ through $\mathrm{d}T_{\mathrm{IR}}/\mathrm{d}T$. This emissivity-engineered amplification allows detection of subtle temperature surface variations that would otherwise fall below the camera's temperature resolution, thereby improving the effective resolution of thermography by a factor of $\mathrm{d}T_{\mathrm{IR}}/\mathrm{d}T$.

Vanadium dioxide (VO₂), known for its thermally induced metal—insulator transition (MIT) at 67 °C, has been widely investigated for emissivity engineering, with several material structures reported to date^{3–8} One notable example is a thermal imaging sensitizer (TIS) based on VO₂-integrated Fabry - Pérot (FP) resonators. The structure exhibits sharp rise in emissivity (from \sim 0.3 to \sim 0.8) within a narrow temperature window (typically 1 – 2 °C) around the MIT, resulting in a pronounced $dT_{\rm IR}/dT$ ratio and enabling millikelvin-resolved thermography near room temperature. However, these FP-based TIS structures are limited in scalability and broader applicability. Their fabrication typically

Received: July 14, 2025 Revised: September 24, 2025

Accepted: September 26, 2025

Published: October 4, 2025





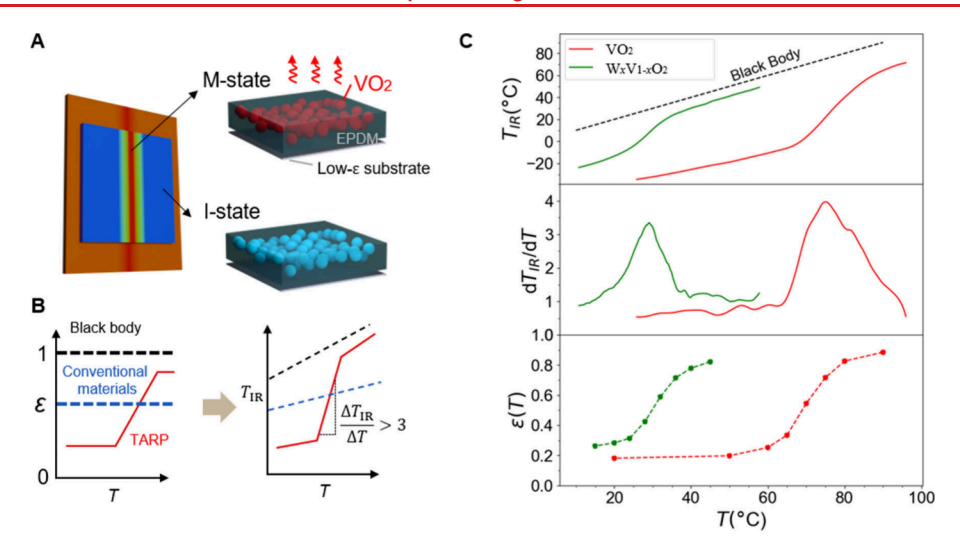


Figure 1. Thermal imaging sensitized by TARP. (A) Schematic illustration of enhanced thermal resolution enabled by TARP. As the object is heated through the MIT, the VO₂ particles in TARP transition from an insulating (I) phase to a metallic (M) phase, increasing the emissivity and thus enhancing the IR imaging contrast. (B) In comparison to conventional materials with constant emissivity, TARP exhibits a step-like emissivity switch across the MIT, in which $T_{\rm IR}$ increases sharply with $T_{\rm IR}$. (C) Measured apparent infrared temperature ($T_{\rm IR}$, top), corresponding thermal amplification ($dT_{\rm IR}/dT$, middle), and emissivity ($\varepsilon(T)$, bottom) as a function of actual temperature (T) for TARP coatings made with VO₂ and $W_xV_{1-x}O_2$ (x=1.5%).

relies on expensive materials and complex nanofabrication processes, limiting both cost-effectiveness and scalability for large-area applications. Moreover, the emissivity switch is highly sensitive to the dielectric spacer thickness, a strict requirement imposed by the FP resonance mechanism. ⁹ The stringent thickness requirement brings significant challenges for large-scale fabrication and limits the potential for further structural optimization. In addition, their high dT_{IR}/dT ratio comes at the cost of a narrow operational temperature range around the MIT temperature, unsuitable for scenarios that require sensitivity over a wider temperature range. To address these limitations, horizontal optical antenna designs have been developed as an alternative to FP structures, removing the strict requirement for spacer thickness control. In addition, the use of roll-to-roll printing offers much higher scalability and reduced fabrication cost.⁶ Despite these advantages, the approach still uses nanofabricated, periodic templates, and yields TIS in the form of unstretchable, solid-state membrane. Recently, a solution-processed VO₂/polymer composite with temperature-adaptive emissivity was reported; however, the emissivity changes only by ~ 0.15 around 67 °C, limiting their practical applications. 10 It would be highly desirable to develop a TIS, with performance comparable to nanofabricated structures, in liquid form that can be painted to any surface, including curved ones, for the broadest range of outdoor applications.

Here, we present a solution-processed, nanoparticles based TIS termed Temperature-Adaptive Radiative Paint (TARP). TARP can be prepared at low cost and large quantity and readily applied onto any solid surfaces to sensitize thermal imaging. It is composed of VO₂ or W-doped VO₂ ($W_xV_{1-x}O_2$) nanoparticles embedded in an infrared-transparent polymer matrix of ethylene-propylene-diene monomer (EPDM). As illustrated in Figure 1A, TARP dynamically modulates its emissivity (ε) in response to temperature changes, enabled by the thermally driven MIT of the VO₂ particles. Thermography measurements demonstrate that TARP effectively boosts dT_{IR}/dT ratio within the MIT temperature range of VO₂ and W-

doped VO₂ (Figure 1C). Unlike nanofabricated or roll-to-roll patterned structures, the VO₂ particles are distributed randomly in TARP, eliminating the need for precise control of spacer layer thickness or interunit distance. This is because ε switches in TARP with a mechanism distinctly different from prior approaches: near-field coupling among adjacent nanoparticles.

■ TARP PREPARATION

The intrinsic MIT temperature (T_{MIT}) of VO₂ is approximately 67 °C, which can be reduced by tungsten doping (W) to fit different applications. For example, doping with 1.5% W reduces T_{MIT} to about 28 °C, making it suitable for ambient applications. 11 In the insulating (I) state at lower temperatures, the particles are largely transparent to mid-IR in the $8-14 \mu m$ wavelength range, 12 and incoming IR radiation will transmit through the VO₂ particles and matrix with negligible absorption and get reflected by the underlying low- ε substrate, which is typically a metal layer such as aluminum. In contrast, when VO₂ transitions to the metallic (M) state at high temperatures, strong interparticle plasmonic resonance will be activated. 13 Consequently, the system undertakes a sharp increase in mid-IR absorbance (A) and hence emissivity, according to Kirchhoff's law of radiation.¹⁴ This step-like emissivity switch of TARP, depicted in Figure 1B (left), drives a drastic increase in the surface thermal radiation upon a small rise in temperature, leading to a steep rise in $T_{\rm IR}$. As shown in Figure 1B (right), the enhanced dT_{IR}/dT boosts thermal imaging sensitivity compared to conventional, constantemissivity materials.

TARP is composed of VO_2 nanoparticles suspended in a polymer matrix. To accommodate both IR transparency and processability, the matrix is prepared by dissolving ethylene-propylene-diene monomer (EPDM) in mineral spirits. Due to its predominant C–C and C–H bonds, EPDM has minimal vibrational absorption across the 8–14 μ m atmospheric window (Figure S1), maximally avoiding optical loss in the spectral range of interest. Is In contrast to other polyolefins

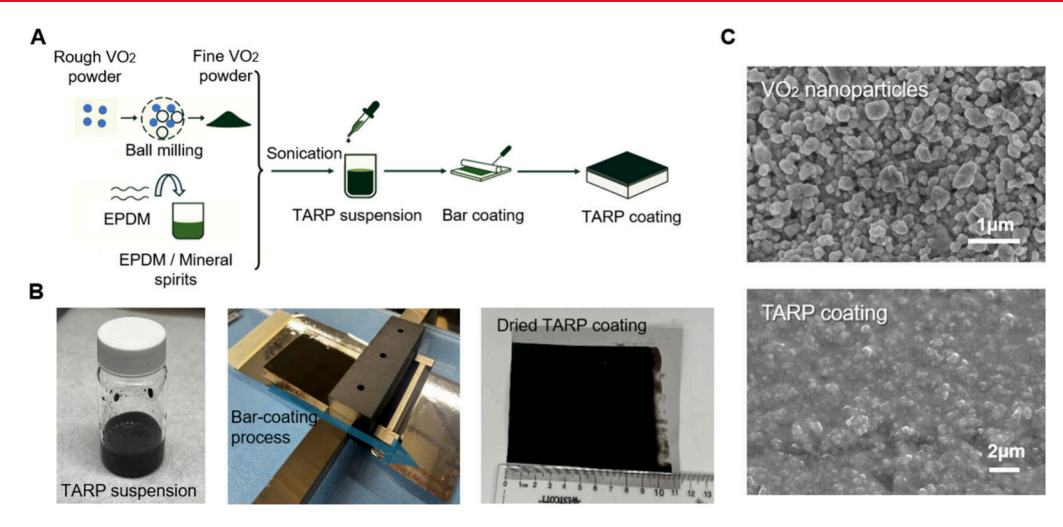


Figure 2. Preparation and morphological characterization of TARP. (A) Schematic illustration of the fabrication workflow. Rough VO₂ powder is first processed via ball milling to produce fine VO₂ nanoparticles. These are then mixed with an EPDM polymer solution (prepared in mineral spirits) and ultrasonicated to form a homogeneous TARP suspension. The suspension is applied to the substrate using a spin-coating or bar-coating method to form uniform TARP films. (B) Photographs showing the prepared TARP suspension (left), the bar-coating process on a substrate (middle), and the resulting, dried TARP film (right). (C) Scanning electron microscopy (SEM) images of the milled VO₂ nanoparticles and surface morphology of the prepared TARP film.

such as polyethylene and polypropylene, EPDM is readily soluble in hydrocarbon solvents such as toluene and mineral spirits, enabling solution-phase processing. Moreover, EPDM is an industrially available material with excellent thermal stability, environmental resistance, and mechanical flexibility, making it an effective binder for scalable and durable coatings. Mineral spirits, a low-aromatic petroleum-derived solvent consisting primarily of C7–C12 aliphatic hydrocarbons, is used to dissolve EPDM. It is widely used in commercial paint systems due to its volatility and solvation power and its reduced aromatic content enhances user safety and environmental compatibility relative to conventional aromatic hydrocarbon solvents.

The optimal VO_2 particle size was calculated through electromagnetic simulations (Figure S2) and produced with high-energy ball milling under controlled conditions. ¹⁷ EPDM was dissolved in mineral spirits to produce a uniform polymer solution, into which the milled VO_2 nanoparticles were incorporated through extended stirring and sonication to ensure uniform and stable dispersion. The resulted formulation was bar-coated onto metal-coated substrates to form a uniform film with controlled thickness on the order of 2.5 μ m (Figure 2A, 2B). This process eliminates the need for lithographic patterning or vacuum deposition, allowing low-cost and scalable manufacturing.

The morphology of the ball-milled VO₂ nanoparticles and the TARP coating was examined by scanning electron microscopy (SEM). The VO₂ nanoparticles have diameters of several hundred nanometers (Figure 2C, top) and are observed to be homogeneously distributed throughout the EPDM matrix (Figure 2C, bottom), confirming uniform and random embedding and film integrity.

PERFORMANCE CHARACTERIZATION AND WORKING MECHANISM

Thermographic characterization was performed with an IR camera which provides the IR temperature readouts ($T_{\rm IR}$) based on the assumption of a constant target emissivity of 0.95. For a surface with constant emissivity, the relationship between

 $T_{\rm IR}$ and T is expected to be approximately linear. Thus, the emergence of a step-like feature in the $T_{\rm IR}-T$ curve indicates a sharp rise in the emissivity of TARP (Figure 1C). Taking the derivative of the $T_{\rm IR}$ profile with respect to T yields the $dT_{\rm IR}/dT$ curve, which quantifies TARP's ability to amplify small temperature variations. As shown in Figure 1B, TARP fabricated with pure VO₂ delivers a peak amplification of $dT_{\rm IR}/dT > 4$ near 75 °C, and maintains values above 3 within the temperature range of 70 - 80 °C. In comparison, TARP with $W_xV_{1-x}O_2$ (x=1.5%) achieves a $dT_{\rm IR}/dT > 3$ around 28 °C, which stays above 2.5 within 25 - 32 °C. These results demonstrate effective enhancement of thermal imaging sensitivity over a relatively broad temperature range.

Spectral reflectance $r(\lambda,T)$ was measured using a Fourier transform infrared (FTIR) spectrometer. Given that TARP is coated on a totally opaque substrate, the spectral thermal emissivity $\varepsilon(\lambda,T)$ was calculated as $1 - r(\lambda,T)$. The effective integrated emissivity $\varepsilon(T)$ was determined by integrating $\varepsilon(\lambda,T)$ weighted by the blackbody spectral radiance $B(\lambda,T)$ according to

$$\varepsilon(T) = \frac{\int \varepsilon(\lambda, T)B(\lambda, T) \, d\lambda}{\int B(\lambda, T) \, d\lambda}$$
(2)

The integration wavelength range spans 8–14 μ m, which corresponds to the typical operating range of IR cameras. From FTIR spectra (Figure 3D, 3E) and $\varepsilon(T)$ profile (Figure 1C, bottom), a clear trend of progressively increasing emissivity is observed as the temperature rises above the $T_{\rm MIT}$ of VO₂ or W_xV_{1-x}O₂ in the TARP. For TARP made with undoped VO₂, $\varepsilon(T)$ increases from 0.26 at temperatures below \sim 60 °C to 0.88 at temperatures above \sim 80 °C. With 1.5% of tungsten doping, the $\varepsilon(T)$ transition is shifted to a lower temperature range that starts at \sim 20 °C, while retaining a pronounced emissivity switch from 0.30 to 0.85.

To elucidate the emissivity switching mechanism of TARP, finite-element simulations were performed using a model geometry in which VO₂ nanoparticles are embedded within an EPDM matrix and arranged in a periodic array with

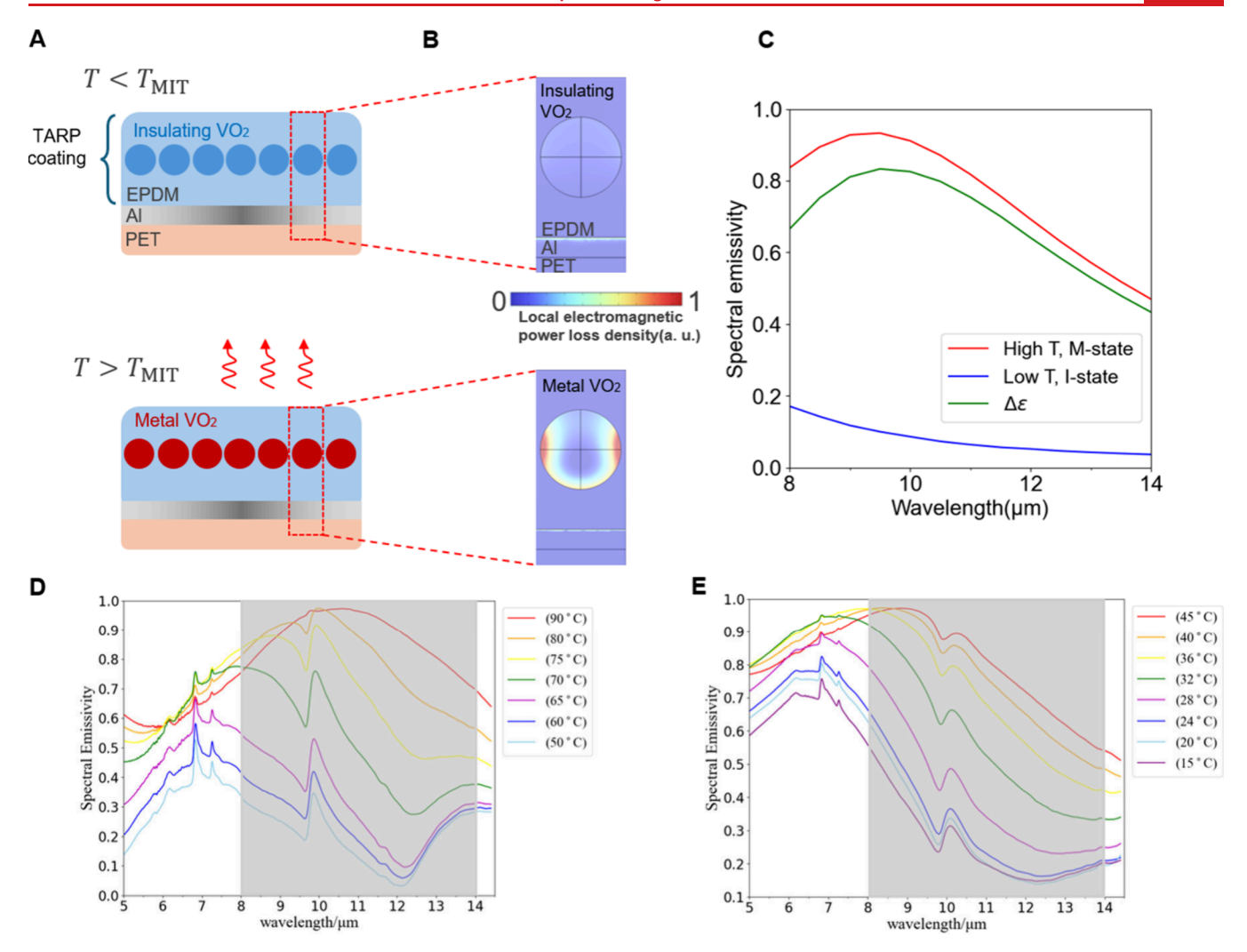


Figure 3. Working mechanism of TARP. (A) Schematic illustration of the emissivity switching mechanism in TARP. (B) Simulated unit cell showing the mid-IR electromagnetic power loss distribution at low and high temperatures. The absorption hot spot is localized at the subwavelength-scale gap between adjacent VO₂ particles, where confinement of the electromagnetic field significantly enhances absorption in the metallic state. The wavelength of the incident light is 10 μ m. (C) Numerically calculated spectral emissivity of TARP in the mid-IR region, comparing high-temperature (M state) and low-temperature (I state) responses, with $\Delta\varepsilon$ representing the change in spectral emissivity. FTIR-resolved temperature-dependent infrared spectra of TARP made with (D) VO₂ and (E) $W_xV_{1-x}O_2$ (x=1.5%). Shaded regions indicate the wavelength ranges used for integrated emissivity calculations.

subwavelength gaps. This structure is positioned atop a midinfrared reflector made of Al-deposited Polyethylene terephthalate (PET) film (Figure 3A).

When temperature T is below $T_{\rm MIT}$, the VO₂ particles are in the insulating phase and exhibit low absorption in the thermal IR range (8–14 μ m), leading to a low emissivity. Above $T_{\rm MIT}$, VO_2 transitions to the metal phase with a large imaginary part of permittivity in the mid-IR.³ In this state, the closely spaced particles—separated by nanoscale gaps which are significantly smaller than the wavelength of interest—support strong near-field electromagnetic coupling. This near-field interaction leads to spatial confinement of electromagnetic fields between adjacent particles, markedly enhancing light-matter interaction and driving efficient broadband absorption, which results in high emissivity at high T. As shown in Figure 3B, absorption hot spots are concentrated at the particle edges facing each other, where field confinement is strongest. Consequently, the simulated spectral emissivity (Figure 3C) exhibits a broad absorption band across the wavelength range, activated upon the phase transition to the M state.

Notably, simulations conducted on systems with realistic TARP model (Figure S3) with same film thickness and volume fraction yield similar results, confirming that the emissivity switching is governed by interparticle photonic activities rather than by long-range periodicity. Moreover, comparing the simulated TARP model and measured spectral emissivity profile of real TARP (Figure 3D, 3E) reveals a very similar curve shape and switching trend, indicating the robustness of the simulation.

■ DEMONSTRATION OF APPLICATIONS

Thermography is widely employed for the inspection of power electronics, offering noninvasive, real-time monitoring of temperature distribution.²² In high-voltage transmission lines, for example, thermal imaging facilitates early detection of structural and electrical anomalies—such as broken strands, corroded conductors, or high-resistance contact points—by identifying localized hot spots.²³ Early stage detection enables timely intervention, reduces maintenance costs, and mitigates the risk of fire or catastrophic failure, thereby extending the

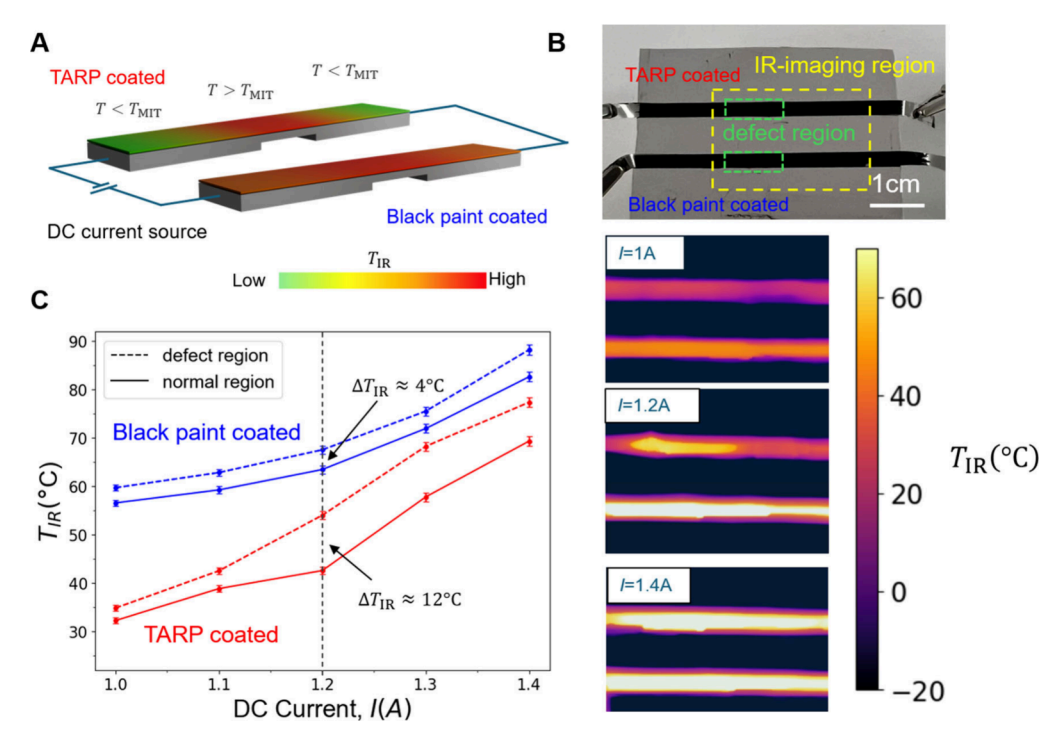


Figure 4. Thermographic detection of hot spots in power electronics using TARP. (A) Schematic of the experimental setup showing two stainless-steel strips with a recess on the backside to simulate a defect, coated with either TARP or black paint, and connected to a DC current source. The defective regions exhibit localized Joule heating due to increased electrical resistance. (B) Optical image of the experimental setup and corresponding IR thermographs acquired at increasing current levels (1.0, 1.2, and 1.4 A), demonstrating localized emissivity switching in the TARP-coated strip which increases thermal contrast. (C) $T_{\rm IR}$ profile of defect and normal regions on both strips as a function of applied DC current (I). As indicated by the black dashed line, at I = 1.2 A, the TARP-coated strip displays a substantially greater temperature contrast ($\Delta T_{\rm IR} \approx 10^{\circ}$ C) compared to that of the black paint ($\Delta T_{\rm IR} \approx 10^{\circ}$ C) near the VO₂ phase transition threshold.

service lifetime of critical infrastructure. Under standard operating conditions, the surface temperature of transmission cables typically hovers around 65 °C. Localized defects often result in modest temperature increases that fall within the emissivity switching range of VO₂-based TARP coatings. Based on this insight, we designed a demonstration to showcase the potential of TARP for early detection of hot spots in transmission lines.

A schematic of the experimental setup is presented in Figure 4A. Two identical stainless-steel strips were prepared, each with an artificially introduced recess on the backside to mimic hidden defects in power transmission lines. One strip was coated with TARP, while the other was coated with conventional black acrylic paint to serve as a reference with constant emissivity of 0.95. Both samples were connected in series to a direct current (DC) source to induce resistive (Joule) heating. The defective region, having higher electrical resistance, exhibited more local heating relative to the normal region. For the TARP-coated sample, this subtle temperature difference was significantly amplified, producing an enhanced contrast of $T_{\rm IR}$ with respect to the normal region.

At low currents, the temperature across both the defective and normal regions remained below the phase-transition threshold of VO_2 , resulting in minimal emissivity difference and indistinct thermal contrast. As the current increases, the temperature of the defective region on the TARP-coated strip enters the temperature window (60–70 °C) of MIT of the VO_2 particles, while the normal region remains below it. This induced a phase transition in the TARP coated on the defective region, boosting emissivity there. Consequently, a clear $T_{\rm IR}$ contrast becomes observable in the thermal image

(Figure 4B). Upon further increasing of the current, the normal region eventually also exceeds the transition temperature window. As a result, the emissivity became uniformly high in both the defective and normal regions.

Moreover, thermography offers a nondestructive means for detecting subsurface structural defects of a wall by monitoring spatial temperature variation on its surface. ^{24,25} Internal anomalies such as voids or cracks can locally perturb thermal conduction or heat capacity, generating measurable temperature gradients. By analyzing these thermal signatures, thermography enables early detection of hidden defects without invasive probing, making thermography a valuable diagnostic tool across aerospace, civil engineering, and manufacturing quality control.

To evaluate the potential of TARP in improving detectability of subsurface defects, a model experiment was conducted using a wood board (thickness ~ 5 mm) containing a concealed groove (depth ~ 3 mm and width ~ 1 mm) on its backside. As schematically shown in Figure 5A, the wood board was placed on a hot plate to simulate a perpendicular temperature gradient, representing temperature differences between (for example) indoor and outdoor environments. The embedded groove introduces a small air gap, whose low thermal conductivity relative to the surrounding wood suppresses heat transfer and results in a slightly reduced surface temperature directly above the groove (Figure S4).

As shown in Figure 5B, a layer of TARP fabricated using $W_xV_{1-x}O_2$ (x=1.5%), with a phase transition temperature near 28 °C, was coated onto a low-emissivity Al/PET foil and subsequently laminated across the top surface of the wood board, spanning the groove (indicated by the green dotted

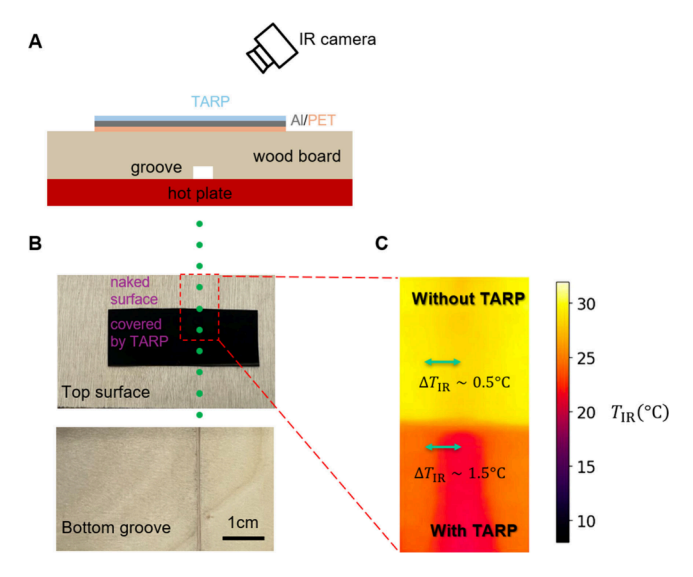


Figure 5. Demonstration of TARP for thermal imaging of concealed structural defects. (A) Schematic of experimental configuration (side view). A groove is introduced on the bottom surface of a wood board, which is then placed on a hot plate to generate a vertical thermal gradient. The top surface is partially covered with a TARP coating laminated onto Al/PET. (B) Optical image showing the location of the subsurface groove (the green dotted line) and IR imaging field of view (red dashed box). (C) Infrared thermograph. The TARP-coated region exhibits enhanced IR temperature contrast ($\Delta T_{\rm IR} \approx 1.5~{}^{\circ}{\rm C}$), enabling clear visualization of the hidden groove, whereas the uncoated region shows only weak contrast ($\Delta T_{\rm IR} \approx 0.5~{}^{\circ}{\rm C}$).

line). The top image in Figure 5B shows the laminated region (labeled "covered by TARP") adjacent to a bare wood surface ("naked surface"), enabling direct comparison. The bottom image displays the underside of the board with the groove.

The system was heated slightly above room temperature to operate within the emissivity switching range (25–32 °C) of the TARP. As shown in the infrared image (Figure 5C), the naked wood surface exhibits a small, barely detectable $T_{\rm IR}$ contrast of ~ 0.5 °C at the groove location. In contrast, the TARP-coated region shows an amplified $T_{\rm IR}$ contrast of ~ 1.5 °C, rendering the backside groove clearly visible in the thermal image. These results demonstrate the capability of TARP enhancing thermographic sensitivity to subsurface structural defects.

In this work, we have developed a temperature-adaptive radiative paint (TARP) that is fully solution-processable from low-cost materials and compatible with scalable coating techniques. The emissivity-switching behavior arises from near-field photonic resonance among VO_2 or $W_xV_{1-x}O_2$ nanoparticles randomly embedded in an infrared-transparent polymer matrix. This mechanism eliminates the need for lithographic patterning or periodic photonic structures typically required in prior temperature-adaptive radiative designs.

The TARP coating improves sensitivity of infrared imaging by amplifying small temperature variations, achieving $\mathrm{d}T_{\mathrm{IR}}/\mathrm{d}T$ of 3 \sim 4 over a temperature window of approximately 10 °C. The performance enables thermographic applications that demand high temperature sensitivity in diverse operating conditions. Proof-of-concept experiments demonstrate the effectiveness of TARP for thermographic inspection of power electronics components and concealed structural defects.

The emissivity-switching performance of TARP could be further improved by using VO₂ or $W_xV_{1-x}O_2$ nanoparticles with higher quality and narrower distribution in size and composition. Enhanced switching sharpness would allow TARP to achieve higher amplification factor, expanding its applicability to cases that demand high thermographic sensitivity. In addition, further electromagnetic simulations may provide insights into optimal particle geometry and distribution configuration. When integrated with a solar reflecting layer on the top, TARP may also play an important role in the field of smart radiative cooling.

ASSOCIATED CONTENT

Supporting Information

The Supporting Information is available free of charge at https://pubs.acs.org/doi/10.1021/acs.nanolett.5c03631.

More details for the material synthesis, thermal imaging and FTIR measurement setup, SEM characterization, numerical simulation setup, and Figures S1–S4 (PDF)

AUTHOR INFORMATION

Corresponding Author

Junqiao Wu — Department of Materials Science and Engineering, University of California, Berkeley, California 94720, United States; Materials Sciences Division, Lawrence Berkeley National Laboratory, Berkeley, California 94720, United States; orcid.org/0000-0002-1498-0148; Email: wuj@berkeley.edu

Authors

Kai Xu — Department of Materials Science and Engineering, University of California, Berkeley, California 94720, United States; Materials Sciences Division, Lawrence Berkeley National Laboratory, Berkeley, California 94720, United States

Jiachen Li — Department of Materials Science and Engineering, University of California, Berkeley, California 94720, United States; Materials Sciences Division, Lawrence Berkeley National Laboratory, Berkeley, California 94720, United States; ⊚ orcid.org/0000-0002-0368-3551

Finnegan G. Reichertz – Department of Materials Science and Engineering, University of California, Berkeley, California 94720, United States; Materials Sciences Division, Lawrence Berkeley National Laboratory, Berkeley, California 94720, United States

Ruihan Guo – Department of Materials Science and Engineering, University of California, Berkeley, California 94720, United States; Materials Sciences Division, Lawrence Berkeley National Laboratory, Berkeley, California 94720, United States; orcid.org/0000-0002-9724-396X

Nawel S. Khelfallah — California Research Alliance (CARA), BASF Corporation, Berkeley, California 94720, United States Rui Zhang — California Research Alliance (CARA), BASF Corporation, Berkeley, California 94720, United States

Ali Javey — Materials Sciences Division, Lawrence Berkeley National Laboratory, Berkeley, California 94720, United States; Electrical Engineering and Computer Sciences and Kavli Energy Nano Science Institute, University of California, Berkeley, California 94720, United States

Rayne Zheng – Department of Materials Science and Engineering, University of California, Berkeley, California 94720, United States

Complete contact information is available at: https://pubs.acs.org/10.1021/acs.nanolett.5c03631

Notes

The authors declare no competing financial interest.

ACKNOWLEDGMENTS

This work was supported by a research grant from BASF via the California Research Alliance (CARA). The FTIR measurements were supported by the U.S. Department of Energy, Office of Science, Office of Basic Energy Sciences, Materials Sciences and Engineering Division, under Contract DE-AC02-05CH11231 (EMAT program KC1201).

REFERENCES

- (1) Niklaus, F.; Vieider, C.; Jakobsen, H. In MEMS-Based Uncooled Infrared Bolometer Arrays: A Review; Chiao, J.-C., Chen, X., Zhou, Z., Li, X., Eds.; 2007; p 68360D.
- (2) Tang, K.; Dong, K.; Nicolai, C. J.; Li, Y.; Li, J.; Lou, S.; Qiu, C.-W.; Raulet, D. H.; Yao, J.; Wu, J. Millikelvin-Resolved Ambient Thermography. *Sci. Adv.* **2020**, *6* (50), No. eabd8688.
- (3) Barker, A. S.; Verleur, H. W.; Guggenheim, H. J. Infrared Optical Properties of Vanadium Dioxide Above and Below the Transition Temperature. *Phys. Rev. Lett.* **1966**, *17* (26), 1286–1289.
- (4) Liu, K.; Lee, S.; Yang, S.; Delaire, O.; Wu, J. Recent Progresses on Physics and Applications of Vanadium Dioxide. *Mater. Today* **2018**, 21 (8), 875–896.
- (5) Tang, K.; Wang, X.; Dong, K.; Li, Y.; Li, J.; Sun, B.; Zhang, X.; Dames, C.; Qiu, C.; Yao, J.; Wu, J. A Thermal Radiation Modulation Platform by Emissivity Engineering with Graded Metal-Insulator Transition. *Adv. Mater.* **2020**, *32* (36), 1907071.
- (6) Li, J.; Dong, K.; Zhang, T.; Tseng, D.; Fang, C.; Guo, R.; Li, J.; Xu, Y.; Dun, C.; Urban, J. J.; Hong, T.; Grigoropoulos, C. P.; Javey, A.; Yao, J.; Wu, J. Printable, Emissivity-Adaptive and Albedo-Optimized Covering for Year-Round Energy Saving. *Joule* **2023**, 7 (11), 2552–2567.
- (7) Wang, S.; Jiang, T.; Meng, Y.; Yang, R.; Tan, G.; Long, Y. Scalable Thermochromic Smart Windows with Passive Radiative Cooling Regulation. *Science* (1979) **2021**, 374 (6574), 1501–1504.
- (8) Tang, K.; Dong, K.; Li, J.; Gordon, M. P.; Reichertz, F. G.; Kim, H.; Rho, Y.; Wang, Q.; Lin, C.-Y.; Grigoropoulos, C. P.; Javey, A.; Urban, J. J.; Yao, J.; Levinson, R.; Wu, J. Temperature-Adaptive Radiative Coating for All-Season Household Thermal Regulation. *Science* (1979) **2021**, 374 (6574), 1504–1509.
- (9) Hodgson, N.; Weber, H. The Fabry Perot Resonator. In *Optical Resonators*; Springer: London, 1997; pp 137–162.
- (10) Si, X.; Zhu, H.; Yang, Z.; Wei, H.; Chen, B.; Wang, R.; Bao, R.; Gu, J.; Zhan, Y. Adaptive Radiative Cooling via Spectral Decoupling in Bilayered Polymer/VO₂ NP Nanocomposites. *ACS Appl. Mater. Interfaces* **2025**, *17* (8), 12117–12124.
- (11) Lee, S.; Hippalgaonkar, K.; Yang, F.; Hong, J.; Ko, C.; Suh, J.; Liu, K.; Wang, K.; Urban, J. J.; Zhang, X.; Dames, C.; Hartnoll, S. A.; Delaire, O.; Wu, J. Anomalously Low Electronic Thermal Conductivity in Metallic Vanadium Dioxide. *Science* (1979) **2017**, 355 (6323), 371–374.
- (12) Beaini, R.; Baloukas, B.; Loquai, S.; Klemberg-Sapieha, J. E.; Martinu, L. Thermochromic VO₂-Based Smart Radiator Devices with Ultralow Refractive Index Cavities for Increased Performance. *Sol. Energy Mater. Sol. Cells* **2020**, 205, 110260.
- (13) Matsui, H.; Ho, Y.; Kanki, T.; Tanaka, H.; Delaunay, J.; Tabata, H. Mid-infrared Plasmonic Resonances in 2D VO₂ Nanosquare Arrays. *Adv. Opt Mater.* **2015**, 3 (12), 1759–1767.
- (14) Kirchhoff, G. I. On the Relation between the Radiating and Absorbing Powers of Different Bodies for Light and Heat. London, Edinburgh, and Dublin Philosophical Magazine and Journal of Science 1860, 20 (130), 1–21.

- (15) Gunasekaran, S.; Natarajan, R. K.; Kala, A. FTIR Spectra and Mechanical Strength Analysis of Some Selected Rubber Derivatives. *Spectrochim Acta A Mol. Biomol Spectrosc* **2007**, *68* (2), 323–330.
- (16) Costa, N. L.; Hiranobe, C. T.; Cardim, H. P.; Dognani, G.; Sanchez, J. C.; Carvalho, J. A. J.; Torres, G. B.; Paim, L. L.; Pinto, L. F.; Cardim, G. P.; Cabrera, F. C.; dos Santos, R. J.; Silva, M. J. A Review of EPDM (Ethylene Propylene Diene Monomer) Rubber-Based Nanocomposites: Properties and Progress. *Polymers (Basel)* 2024, 16 (12), 1720.
- (17) Wang, C.; Xu, H.; Liu, T.; Yang, S.; Nie, Y.; Wang, C.; Guo, X.; Wang, B.; Ma, X.; Jiang, X. One-Step Ball Milling Synthesis of VO₂ (M) Nanoparticles with Exemplary Thermochromic Performance. SN Appl. Sci. **2021**, 3 (4), 436.
- (18) Le, F.; Brandl, D. W.; Urzhumov, Y. A.; Wang, H.; Kundu, J.; Halas, N. J.; Aizpurua, J.; Nordlander, P. Metallic Nanoparticle Arrays: A Common Substrate for Both Surface-Enhanced Raman Scattering and Surface-Enhanced Infrared Absorption. *ACS Nano* **2008**, 2 (4), 707–718.
- (19) Khattak, H. K.; Bianucci, P.; Slepkov, A. D. Linking Plasma Formation in Grapes to Microwave Resonances of Aqueous Dimers. *Proc. Natl. Acad. Sci. U. S. A.* **2019**, *116* (10), 4000–4005.
- (20) Flory, F. Optical Properties of Nanostructured Materials: A Review. J. Nanophotonics 2011, 5 (1), 052502.
- (21) Wang, H.; Kundu, J.; Halas, N. J. Plasmonic Nanoshell Arrays Combine Surface-Enhanced Vibrational Spectroscopies on a Single Substrate. *Angew. Chem., Int. Ed.* **2007**, *46* (47), 9040–9044.
- (22) Jadin, M. S.; Taib, S. Recent Progress in Diagnosing the Reliability of Electrical Equipment by Using Infrared Thermography. *Infrared Phys. Technol.* **2012**, *55* (4), 236–245.
- (23) Mechkov, E. Application of Infrared Thermography Technique in Transformers Maintenance in Distribution Network. In 2017 15th International Conference on Electrical Machines, Drives and Power Systems (ELMA); IEEE, 2017; pp 354–357.
- (24) Milovanović, B.; Banjad Pečur, I. Review of Active IR Thermography for Detection and Characterization of Defects in Reinforced Concrete. J. Imaging 2016, 2 (2), 11.
- (25) Miao, L.; Gao, B.; Li, H.; Lu, X.; Liu, L.; Woo, W. L.; Wu, J. Novel Interventional Electromagnetic Thermography for Subsurface Defect Detection. *International Journal of Thermal Sciences* **2023**, 184, 107960.